

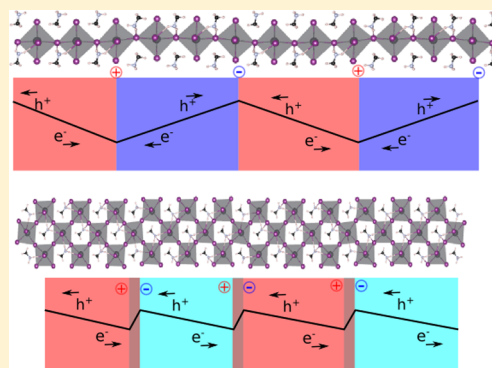
## Ferroelectric Domain Wall Induced Band Gap Reduction and Charge Separation in Organometal Halide Perovskites

Shi Liu, Fan Zheng, Nathan Z. Koocher, Hiroyuki Takenaka, Fenggong Wang, and Andrew M. Rappe\*

The Makineni Theoretical Laboratories, Department of Chemistry, University of Pennsylvania, Philadelphia, Pennsylvania 19104–6323, United States

## S Supporting Information

**ABSTRACT:** Organometal halide perovskites have been intensely studied in the past 5 years, inspired by their certified high photovoltaic power conversion efficiency. Some of these materials are room-temperature ferroelectrics. The presence of switchable ferroelectric domains in methylammonium lead triiodide,  $\text{CH}_3\text{NH}_3\text{PbI}_3$ , has recently been observed via piezoresponse force microscopy. Here, we focus on the structural and electronic properties of ferroelectric domain walls in  $\text{CH}_3\text{NH}_3\text{PbX}_3$  ( $\text{X} = \text{Cl}, \text{Br}, \text{I}$ ). We find that organometal halide perovskites can form both charged and uncharged domain walls due to the flexible orientational order of the organic molecules. The electronic band gaps for domain structures possessing  $180^\circ$  and  $90^\circ$  walls are estimated with density functional theory. It is found that the presence of charged domain walls will significantly reduce the band gap by 20–40%, while the presence of uncharged domain walls has no substantial impact on the band gap. We demonstrate that charged domain walls can serve as segregated channels for the motions of charge carriers. These results highlight the importance of ferroelectric domain walls in hybrid perovskites for photovoltaic applications and suggest a possible avenue for device optimization through domain patterning.



The studies of organometal halide perovskites date back over a century.<sup>1,2</sup> Their applications in photovoltaic devices have seen amazing improvements in the past 5 years. In 2006, the device based on methylammonium lead tribromide,  $\text{CH}_3\text{NH}_3\text{PbBr}_3$ , had a power conversion efficiency of 2.2%.<sup>3</sup> Methylammonium lead triiodide ( $\text{CH}_3\text{NH}_3\text{PbI}_3$ ) was later introduced as a light sensitizer in dye-sensitized solar cells by Kojima and co-workers in 2009, leading to an efficiency of 3.8%.<sup>4</sup> Since then, the power conversion efficiency of photovoltaic devices based on organometal halide perovskites has increased rapidly to nearly 20%.<sup>5,6</sup> The high efficiency of  $\text{CH}_3\text{NH}_3\text{PbI}_3$ <sup>7</sup> and its chlorine-doped derivative  $\text{CH}_3\text{NH}_3\text{PbI}_{3-x}\text{Cl}_x$ <sup>8,9</sup> is the result of their near-optimal direct band gap ( $\sim 1.55$  eV),<sup>4,10</sup> high optical absorption,<sup>11,12</sup> high carrier mobility,<sup>8,13–17</sup> and long carrier diffusion length.<sup>18</sup> Some organometal halide perovskites also exhibit room-temperature ferroelectricity.<sup>19</sup> First-principles density functional theory (DFT) calculations show a strong bulk polarization in  $\text{CH}_3\text{NH}_3\text{PbI}_3$ .<sup>20</sup> Recent DFT calculations demonstrate that the orientational order of the methylammonium (MA) cations will influence the magnitude of bulk polarization.<sup>21,22</sup> It is suggested that the spontaneous polarization within these materials may enhance the charge separation and help achieve above-band-gap open-circuit voltages.<sup>20,23,24</sup>

Ferroelectric materials usually possess complex domain structures, with domain walls separating regions of homogeneously polarized domains. The domain wall is considered to

be a 2D topological defect and has been widely studied in inorganic ferroelectrics.<sup>25–31</sup> It has been demonstrated that domain walls can exhibit distinct electronic properties that are different from bulk materials.<sup>32,33</sup> The presence of switchable ferroelectric domains in  $\beta\text{-CH}_3\text{NH}_3\text{PbI}_3$  has been confirmed recently via piezoresponse force microscopy.<sup>19</sup> However, the local structure and the electronic properties of domain walls in organometal halide perovskites remain unknown. In this Letter, we explore the energies and electronic structures of  $180^\circ$  and  $90^\circ$  domain walls in  $\text{MAPbX}_3$  ( $\text{MA} = \text{CH}_3\text{NH}_3$ ,  $\text{X} = \text{Cl}, \text{Br}, \text{I}$ ) via DFT. Both types of domain walls can be charged or uncharged, depending on the orientational order of the organic molecules around the domain boundaries. We find that a domain structure with charged walls will have a lower band gap than that of a single domain (SD). On the contrary, the presence of uncharged walls has little impact on the band gap. Our calculations demonstrate the importance of these 2D topological defects and suggest a potential avenue to tune the band gap via domain engineering.

For our calculations, we have used the plane-wave DFT package QUANTUM-ESPRESSO<sup>34</sup> with the Perdew–Burke–Ernzerhof (PBE)<sup>35</sup> density functional and optimized norm-conserving pseudopotentials generated from the OPIUM

Received: December 17, 2014

Accepted: January 22, 2015

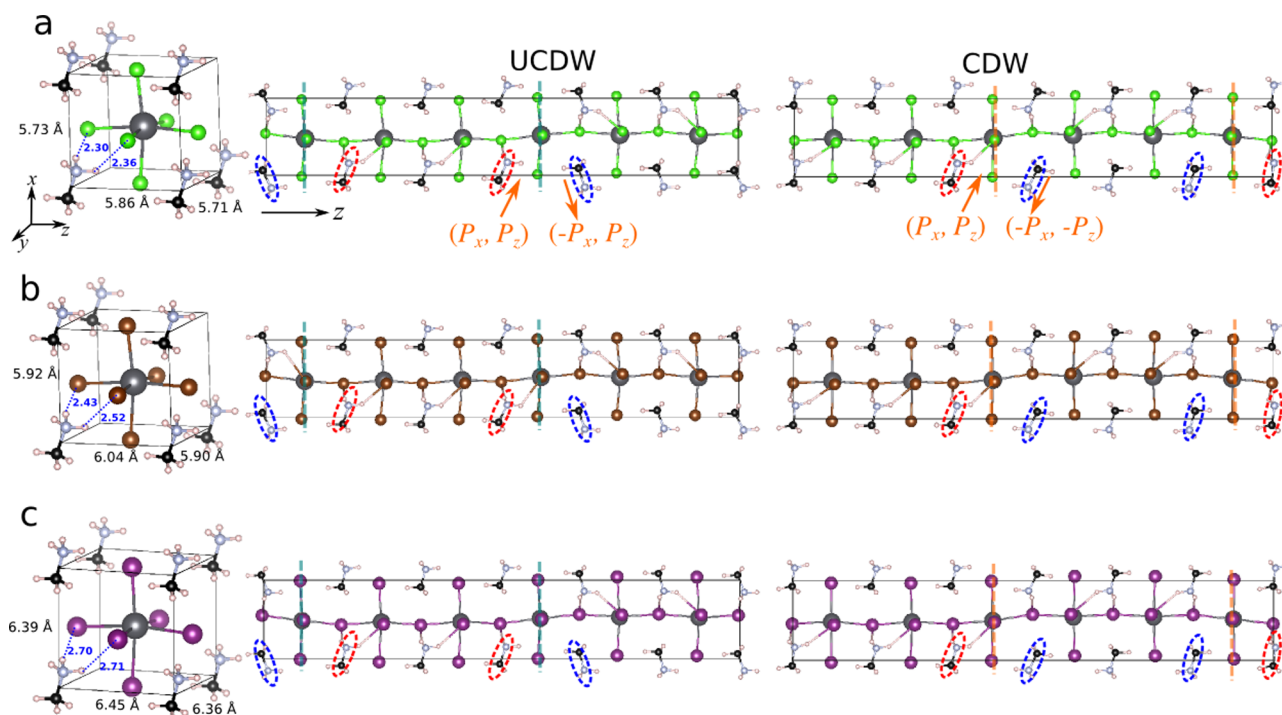


**Figure 1.** Optimized orthorhombic unit cells and domain structures with  $180^\circ$  domain walls in (a) MAPbCl<sub>3</sub>, (b) MAPbBr<sub>3</sub>, and (c) MAPbI<sub>3</sub>. The left panel is the relaxed orthorhombic unit cell. The middle panel is the side view of a  $1 \times 1 \times 6$  supercell containing  $180^\circ$  uncharged domain walls (UCDWs); the polarization changes from  $(P_x, P_z)$  to  $(-P_x, P_z)$ , as demonstrated with orange arrows. The right panel is the side view of a supercell with  $180^\circ$  charged domain walls (CDWs); the polarization changes from  $(P_x, P_z)$  to  $(-P_x, -P_z)$ . The X $\cdots$ H–N hydrogen bond is displayed explicitly to help the visualization of different domains. Pb: dark gray; I: purple; Br: brown; Cl: green; C: black; N: light blue; H: light pink.

package.<sup>36,37</sup> According to previous computational studies, a plane-wave cutoff energy of 50 Ry is used.<sup>22</sup> We first optimize the geometry of the orthorhombic 12-atom unit cell of MAPbX<sub>3</sub> (X=Cl, Br, I) with an  $8 \times 8 \times 8$  Monkhorst–Pack  $k$ -point grid.<sup>38</sup> Figure 1 shows the optimized orthorhombic unit cells for MAPbX<sub>3</sub>. Using Berry phase calculations, we find that the polarization, aligning with the molecular dipoles, is mostly along the  $x$  axis ( $P_x$ ) with a value of 0.13 C/m<sup>2</sup> for MAPbCl<sub>3</sub>, 0.12 C/m<sup>2</sup> for MAPbBr<sub>3</sub>, and 0.12 C/m<sup>2</sup> for MAPbI<sub>3</sub>. The hydrogen bond between the  $-\text{NH}_3$  group and the halogen atom is critical for the bulk polarization. Additionally, as the dipoles of the MA cations are not perfectly aligned along the  $x$  axis, the unit cell has a small component of polarization ( $\sim 0.04$  C/m<sup>2</sup>) along the  $z$  direction ( $P_z$ ), as shown in Figure 1a–c. For the simulation of the  $180^\circ$  domain wall, we use a supercell consisting of  $1 \times 1 \times 6$  orthorhombic unit cells stacked along the  $z$  direction. The uncharged domain wall (UCDW) is constructed by rotating the orientations of MA cations in the right three cells such that the polarization changes from  $(P_x, 0, P_z)$  to  $(-P_x, 0, P_z)$  across the wall. On the other hand, the charged domain wall (CDW) has the polarization change from  $(P_x, 0, P_z)$  to  $(-P_x, 0, -P_z)$  across the domain boundary, with the  $P_z$  component being discontinuous at the domain wall. The dimensions of the supercell are fixed to values based on the optimized lattice constants of the orthorhombic unit cell. The atomic positions are then fully relaxed using a  $3 \times 3 \times 1$  Monkhorst–Pack  $k$ -point mesh. We report in Figure 1 the optimized domain structures with charged and uncharged  $180^\circ$  walls in MAPbI<sub>3</sub>, MAPbBr<sub>3</sub>, and MAPbCl<sub>3</sub>. The domain wall energy ( $E_{\text{DW}}$ ) is calculated by

$$E_{\text{DW}} = \frac{E_{\text{supercell}} - E_{\text{bulk}}}{2S_{\text{DW}}} \quad (1)$$

where  $E_{\text{supercell}}$  is the energy of the supercell containing domain walls and  $E_{\text{bulk}}$  is the energy of a single-domain supercell of the same size (see detailed explanations in the Supporting Information).  $S_{\text{DW}}$  is the domain wall area and is equal to the cross-sectional area of the supercell. It is noted that each supercell includes two domain walls due to the application of periodic boundary conditions. We find that the uncharged wall has small domain wall energies (3 mJ/m<sup>2</sup> in MAPbCl<sub>3</sub>, 1 mJ/m<sup>2</sup> in MAPbBr<sub>3</sub>, and 8 mJ/m<sup>2</sup> in MAPbI<sub>3</sub>). The energies for  $180^\circ$ CDWs in MAPbCl<sub>3</sub>, MAPbBr<sub>3</sub>, and MAPbI<sub>3</sub> are 22, 28, and 33 mJ/m<sup>2</sup>, respectively. These values are comparable to Ti-centered  $180^\circ$  domain walls in BaTiO<sub>3</sub> (17 mJ/m<sup>2</sup>).<sup>39</sup> The relatively low domain wall energy suggests that the formation of both CDWs and UCDWs are energetically possible in hybrid perovskites.

The band gap is a crucial material factor for photovoltaic applications. We calculate the band structures for supercells with and without  $180^\circ$  domain walls. As shown in Table 1, the calculated PBE band gaps for SDs ( $E_{\text{g}}^{\text{bulk}}$ ) are comparable to experimental (e.g., 1.5–1.6 eV for MAPbI<sub>3</sub>)<sup>4,10</sup> and reported theoretical values (e.g., 2.34 eV for MAPbCl<sub>3</sub> with PBE in ref 40).<sup>15,16,40</sup> Surprisingly, we find that domain structures with  $180^\circ$ CDWs have smaller band gaps ( $E_{\text{g}}^{180\text{CDW}}$ ) than their single-domain counterparts, while structures with  $180^\circ$ UCDWs have band gaps ( $E_{\text{g}}^{180\text{UCDW}}$ ) similar to bulk values. Generally, a significant 20% band gap reduction is observed after introducing CDWs spaced by  $\sim 1.5$  nm in MAPbX<sub>3</sub>. A larger supercell of  $1 \times 1 \times 8$  is also employed to study the

**Table 1.** Band gaps ( $E_g$  in eV) for Structures with and without  $180^\circ$  Domain Walls in MAPbX<sub>3</sub>, Calculated with PBE

	$E_g^{\text{bulk}}$	$E_g^{180\text{UCDW}}$	$E_g^{180\text{UCDW}} - E_g^{\text{bulk}}$	$E_g^{180\text{CDW}}$	$E_g^{180\text{CDW}} - E_g^{\text{bulk}}$
PBE					
MAPbCl <sub>3</sub>	2.39	2.38	−0.01	1.89	−0.50
MAPbBr <sub>3</sub>	1.69	1.70	+0.01	1.30	−0.39
MAPbI <sub>3</sub>	1.58	1.56	−0.02	1.29	−0.29
PBE + SOC					
MAPbCl <sub>3</sub>	1.35	1.32	−0.03	0.92	−0.43
MAPbBr <sub>3</sub>	0.67	0.67	+0.00	0.38	−0.29
MAPbI <sub>3</sub>	0.45	0.43	−0.02	0.25	−0.20

charged  $180^\circ$  walls in MAPbI<sub>3</sub>, and a band gap reduction of 0.41 eV is observed. Spin–orbit coupling (SOC) is known to have a profound effect on the electronic structure of organometal halide perovskites;<sup>41–43</sup> therefore, we also evaluate the band gaps with PBE + SOC (Table 1). It is found that the band gaps with SOC are reduced by 0.20 eV in MAPbI<sub>3</sub>, 0.29 eV in MAPbBr<sub>3</sub>, and 0.43 eV in MAPbCl<sub>3</sub> due to CDWs. Figure 2a,b shows the band structures of MAPbI<sub>3</sub> with and without charged  $180^\circ$  walls. The band gap reduction results from the upshift of the valence band maximum (VBM) and the downshift of the conduction band minimum (CBM). Most notably, the presence of  $180^\circ$  walls removes the Rashba band splitting demonstrated in bulk MAPbI<sub>3</sub><sup>44</sup> due to the

recovery of symmetry (net zero polarization) for the whole supercell. The trend in band gap change in MAPbCl<sub>3</sub> is also examined using hybrid functional HSE06<sup>45,46</sup> with SOC. The band gap is reduced from 2.47 eV for the SD to 2.08 eV for the structure with 180UCDW, confirming the trend that we observed with PBE.

In order to understand the origin of the band gap reduction, we analyzed the local density of states (LDOS) for a structure with charged  $180^\circ$  walls in MAPbI<sub>3</sub>. Shown in Figure 3a is the layer-resolved LDOS. The states near the band gap are mainly due to the hybridization between Pb and I atoms. The orbitals from the organic molecules are far away from the band gap, in agreement with previous theoretical work.<sup>15,16</sup> As one can see from the layer-resolved LDOS, the CBM is located at domain wall A (Figure 3 inset) which has  $P_z$  components meeting with a head-to-head configuration, and the VBM is at domain wall B with a tail-to-tail configuration. A head-to-head domain wall has positive bound charges, while a tail-to-tail domain wall has negative bound charges.<sup>47</sup> This will give rise to an electric field across the domain, which is responsible for the shift of the CBM and VBM.<sup>48</sup> The calculated electrostatic potential (potential felt by negative test charge) along the  $z$  direction shown in Figure 3b has a zigzag shape, with domain wall A at the potential minimum and domain wall B at the potential maximum, revealing a built-in electrostatic field due to static uncompensated charges at domain walls. For comparison, we plot the in-plane averaged electronic electrostatic potential

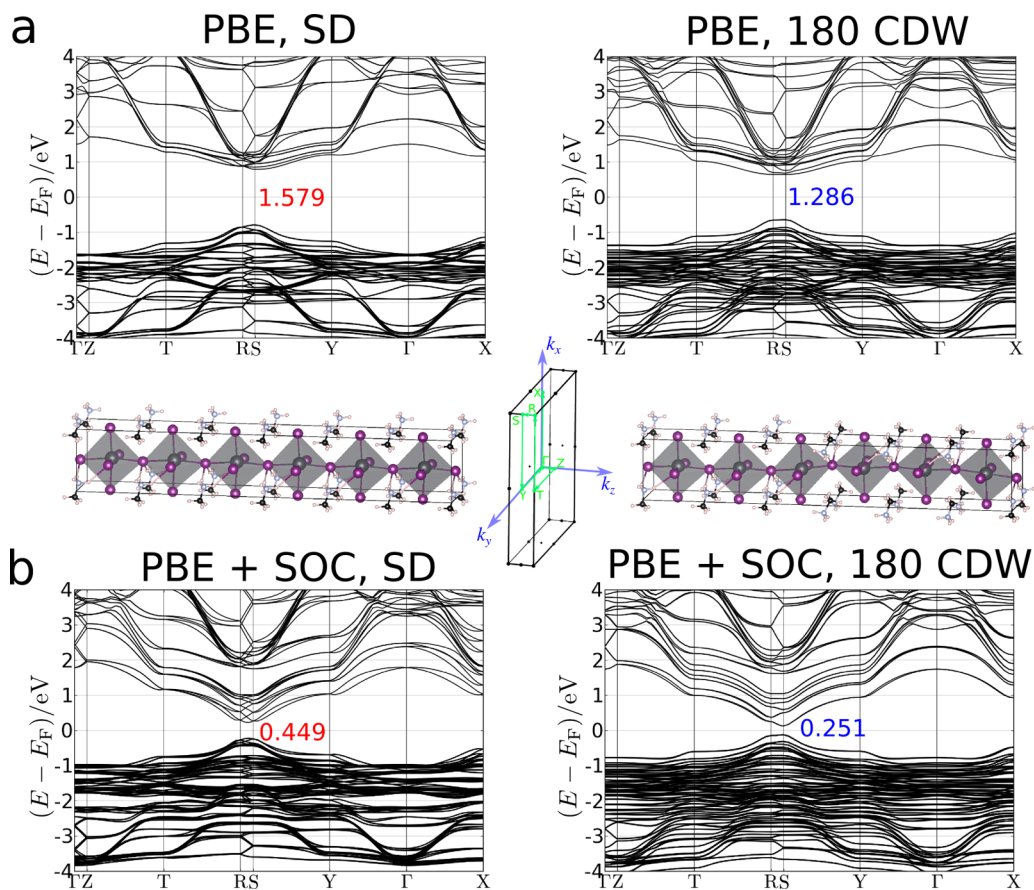


**Figure 2.** Calculated band structures for MAPbI<sub>3</sub> (a) with PBE and (b) with PBE and SOC. The left panel is for a single domain (SD), and the right panel is for structures with charged  $180^\circ$  domain walls (180CDWs). The Brillouin zone and the  $k$ -point path for the  $1 \times 1 \times 6$  supercell are displayed in the middle. Band gap values are in eV.



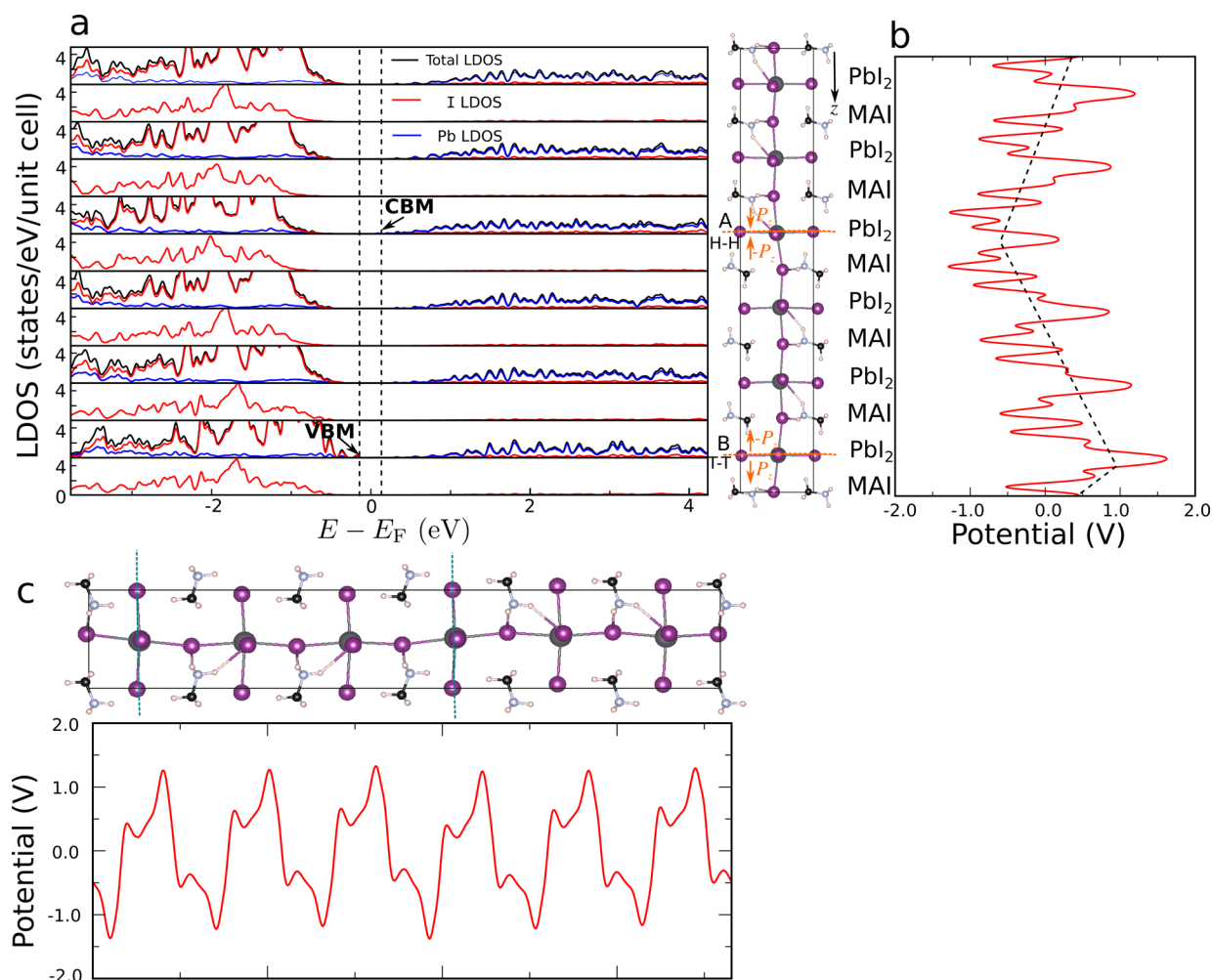


**Figure 3.** (a) Layer-resolved LDOS and (b) electronic electrostatic potential along the  $z$  direction across 180CDWs in MAPbI<sub>3</sub>. The states near the band gap are mainly due to the hybridization between Pb and I atoms. The inset shows the domain structure with 180CDWs labeled as A and B. Domain A has a head-to-head (H–H) configuration (positively charged). Domain B has a tail-to-tail (T–T) configuration (negatively charged). (c) Electronic electrostatic potential across 180UCDWs in MAPbI<sub>3</sub>.

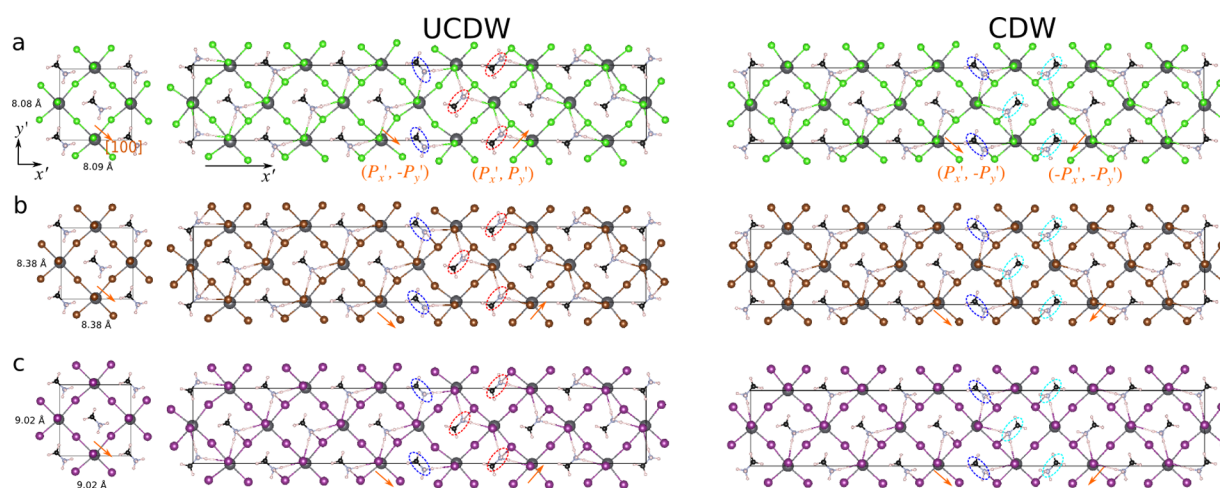


**Figure 4.** Optimized orthorhombic  $\sqrt{2} \times \sqrt{2} \times 1$  unit cells and domain structures with 90° domain walls in (a) MAPbCl<sub>3</sub>, (b) MAPbBr<sub>3</sub>, and (c) MAPbI<sub>3</sub>. The left panel is the relaxed 24-atom unit cell. The middle panel is the side view of a  $6\sqrt{2} \times \sqrt{2} \times 1$  supercell with uncharged 90° walls. The right panel is the side view of a supercell with charged 90° walls. The orange arrows represent the directions of the polarization. The X··H–N hydrogen bond is displayed explicitly to help the visualization of different domains. Pb: dark gray; I: purple; Br: brown; Cl: green; C: black; N: light blue; H: light pink.

for the uncharged  $180^\circ$  walls in Figure 3c. Because the  $P_z$  component is small and continuous across the uncharged  $180^\circ$  walls, a flat averaged potential profile is found.

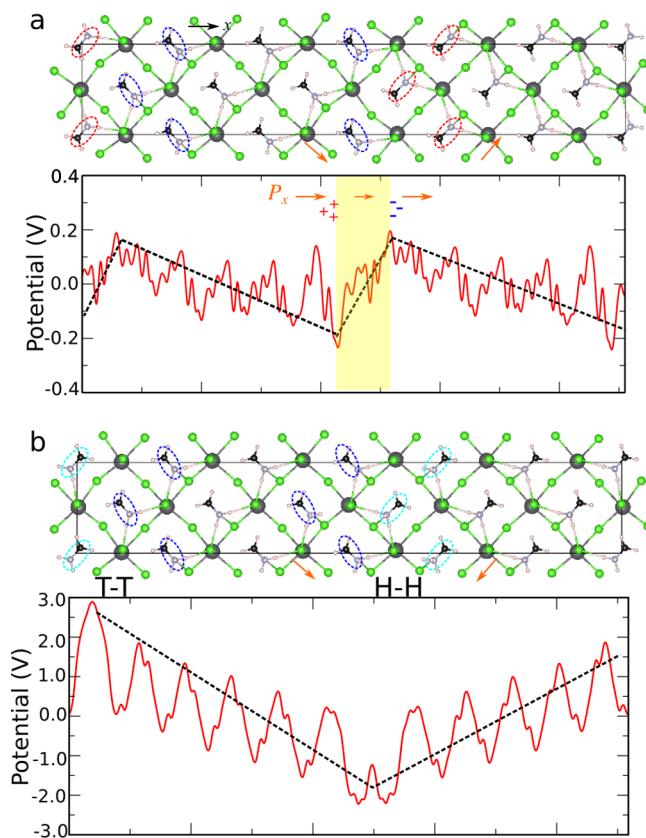
Further, we explore the  $90^\circ$  domain walls in MAPbX<sub>3</sub>. Adopting a strategy similar to that for simulating  $180^\circ$  walls, we first relax the  $\sqrt{2} \times \sqrt{2} \times 1$  unit cell of MAPbX<sub>3</sub>. The structures of optimized unit cells have polarization along [100] ( $P'_x \approx P'_y = (1/\sqrt{2})P_{[100]}$ ) as shown in Figure 4a–c. The domain structure with  $90^\circ$  walls is then constructed by stacking six  $\sqrt{2} \times \sqrt{2} \times 1$  cells along  $x$  while rotating the orientations of MA molecules by  $90^\circ$  in the three unit cells on the right. The polarization changes from  $(P'_x, -P'_y, 0)$  to  $(P'_x, P'_y, 0)$  across the uncharged  $90^\circ$  domain wall (90UCDW) at the [011] plane and from  $(P'_x, -P'_y, 0)$  to  $(-P'_x, -P'_y, 0)$  across the charged  $90^\circ$  domain wall (90CDW). The atomic positions are relaxed with fixed supercell dimensions. It is worth noting that the 90CDW investigated here has the whole  $P'_x$  component head-to-head (tail-to-tail). This configuration is generally not stable in bulk inorganic ferroelectrics due to the large depolarization field at domain walls.<sup>49</sup> It is also possible to construct a charged  $90^\circ$  wall by rotating the  $P'_x$  component such that only a small component is head-to-head (similar to the construction of charged  $180^\circ$  walls).

Figure 4 displays the geometries for the  $90^\circ$  domain walls. The energy differences between structures with and without 90UCDW are small (within 5 meV/formula unit), indicating negligible domain wall energies for the current setup. The energies for 90CDWs in MAPbCl<sub>3</sub>, MAPbBr<sub>3</sub>, and MAPbI<sub>3</sub>, are 66, 54, and 56 mJ/m<sup>2</sup>, respectively. These values, though higher than those for  $180^\circ$ CDWs, are still comparable to those for  $90^\circ$  domain walls in inorganic ferroelectrics such as PbTiO<sub>3</sub>.<sup>39</sup> The results for band structure calculations with PBE and PBE + SOC are summarized in Table 2. It is found that 90CDWs will significantly reduce the band gaps, and 90UCDWs have no impact on the band gaps, consistent with our findings for  $180^\circ$  domain walls. Figure 5 presents the computed potential across  $90^\circ$  domain walls in MAPbCl<sub>3</sub>. For the uncharged  $90^\circ$  walls, the potential decreases along the direction of the  $P'_x$  within each domain. Also noticeable is the potential jump across the domain boundary. This is caused by the dipole layer at the domain wall due to the variation of  $P'_x$  across the boundary (Figure 5a). As for the charged  $90^\circ$  walls, similar to charged  $180^\circ$  walls, the head-to-head wall is at the potential minimum, and the tail-to-tail wall is at the potential maximum.

It is hypothesized that the ferroelectric domains in hybrid halide perovskites may help the separation of photoexcited electrons and holes, and reduce recombination through the segregation of charge carriers.<sup>20</sup> Here, we demonstrate that

**Table 2. Band Gaps for Structures with and without  $90^\circ$  Domain Walls in MAPbX<sub>3</sub> Calculated with PBE**

	$E_g^{\text{bulk}}$	$E_g^{90\text{UCDW}}$	$E_g^{90\text{UCDW}} - E_g^{\text{bulk}}$	$E_g^{90\text{CDW}}$	$E_g^{90\text{CDW}} - E_g^{\text{bulk}}$
PBE					
MAPbCl <sub>3</sub>	2.43	2.45	+0.02	1.62	−0.81
MAPbBr <sub>3</sub>	1.80	1.83	+0.03	1.14	−0.66
MAPbI <sub>3</sub>	1.75	1.70	−0.05	0.96	−0.79
PBE + SOC					
MAPbCl <sub>3</sub>	1.39	1.44	+0.05	1.06	−0.34
MAPbBr <sub>3</sub>	0.78	0.83	+0.05	0.63	−0.15
MAPbI <sub>3</sub>	0.63	0.59	−0.04	0.40	−0.23



**Figure 5.** Electronic electrostatic potential across (a) 90UCDWs and (b) 90CDWs in MAPbCl<sub>3</sub>. The black broken lines are guidelines for eyes.

CDWs, both  $180$  and  $90^\circ$ , can serve as segregated channels for the motion of charge carriers. As illustrated in Figure 6a, electrons prefer to diffuse to head-to-head CDWs, and holes prefer to move to tail-to-tail CDWs. Then, electrons and holes are likely to move separately along different CDWs under internal or external electric fields, reducing the rate of recombination. As for UCDWs, the  $180^\circ$  wall may not result in a strong potential step for electron–hole separation due to the small polarization component along the domain wall normal (Figure 3c). However, 90UCDWs may act as dipole layers and give rise to significant potential steps, helping the

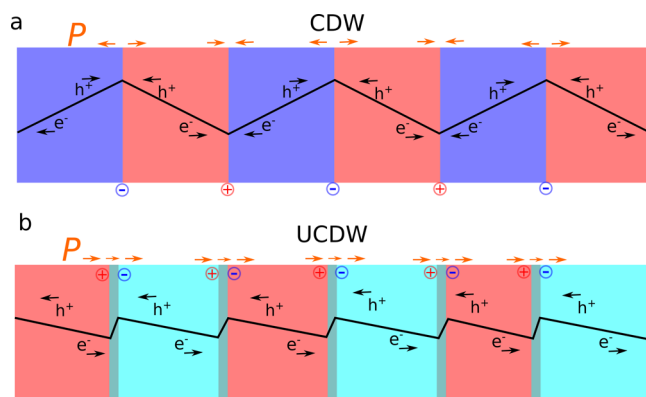


**Figure 6.** Schematic illustrations of electrostatic potential steps and electron–hole separations in a periodic array of (a) CDWs and (b) UCDWs.  $\oplus$  and  $\ominus$  represent bound positive and negative charges.

carrier separation and increasing the diffusion lengths in hybrid halide perovskites (Figure 6b).

In summary, the structural and electronic properties of ferroelectric 180 and 90° domain walls in MAPbCl<sub>3</sub>, MAPbBr<sub>3</sub>, and MAPbI<sub>3</sub> are studied via first-principles DFT. The domain wall energies in these materials are found to be small, suggesting that the formation of domain walls is energetically feasible. Most noticeably, we find that the presence of CDWs (head-to-head and tail-to-tail) will reduce the band gap significantly, while the head-to-tail UCDWs will not induce such reduction. Both 180 and 90° CDWs can serve as segregated channels for the motions of charge carriers. The presence of 90UCDWs may increase the carrier diffusion length. It should be noted that the rotations of PbX<sub>6</sub> octahedra are generally ignored in this investigation, partly due to the associated computational cost. Future investigations are required to fully understand the interplay between orientational order of organic molecules, rotations of inorganic octahedra, and the electronic structure of organometal halide perovskites.<sup>50</sup> It is also of great importance to study the effect of temperature<sup>51–55</sup> on domain walls. Our findings highlight the importance of ferroelectric domain walls in hybrid perovskites and also suggest a promising approach to optimize devices via domain wall engineering.

## ■ ASSOCIATED CONTENT

### ■ Supporting Information

Method for calculating the domain wall energy and OPIUM input files for generating optimized norm-conserving pseudopotentials. This material is available free of charge via the Internet at <http://pubs.acs.org>.

## ■ AUTHOR INFORMATION

### Corresponding Author

\*E-mail: [rappe@sas.upenn.edu](mailto:rappe@sas.upenn.edu).

### Notes

The authors declare no competing financial interest.

## ■ ACKNOWLEDGMENTS

S.L. was supported by the NSF under Grant DMR-1124696. F.Z. was supported by the DOE under Grant DE-FG02-07ER46431. N.Z.K. was supported by the US ONR under Grant N00014-14-1-0761 and by the Roy & Diana Vagelos Scholars Program in the Molecular Life Sciences. H.T. was supported by the U.S. ONR under Grant N00014-12-1-1033. F.W. was supported by the DOE under Grant DE-FG02-07ER46431. A.M.R. was supported by the NSF under Grant CMMI-1334241. Computational support was provided by the U.S. DOD from the HPCMO and by the U.S. DOE at NERSC.

## ■ REFERENCES

- (1) Topsøe, H. Kristallographisch-chemische Untersuchungen Homologer Verbindungen. *Z. Kristallogr.* **1884**, *8*, 246–296.
- (2) Wyckoff, R. The Crystal Structures of Monomethyl Ammonium Chlorostannate and Chloroplatinate. *Am. J. Sci.* **1928**, 349–359.
- (3) Kojima, A.; Teshima, K.; Miyasaka, T.; Shirai, Y. Novel Photoelectrochemical Cell with Mesoscopic Electrodes Sensitized by Lead-Halide Compounds (2). 210th ECS Meeting, Abstract #397, Cancun, Mexico, Oct 29–Nov 3, 2006; pp 397397

- (4) Kojima, A.; Teshima, K.; Shirai, Y.; Miyasaka, T. Organometal Halide Perovskites as Visible-Light Sensitizers for Photovoltaic Cells. *J. Am. Chem. Soc.* **2009**, *131*, 6050–6051.
- (5) Zhou, H.; Chen, Q.; Li, G.; Luo, S.; Song, T.-b.; Duan, H.-S.; Hong, Z.; You, J.; Liu, Y.; Yang, Y. Interface Engineering of Highly Efficient Perovskite Solar Cells. *Science* **2014**, *345*, 542–546.
- (6) Jeon, N. J.; Lee, H. G.; Kim, Y. C.; Seo, J.; Noh, J. H.; Lee, J.; Seok, S. I. *o*-Methoxy Substituents in Spiro-OMeTAD for Efficient Inorganic–Organic Hybrid Perovskite Solar Cells. *J. Am. Chem. Soc.* **2014**, *136*, 7837–7840.
- (7) Burschka, J.; Pellet, N.; Moon, S.-J.; Humphry-Baker, R.; Gao, P.; Nazeeruddin, M. K.; Grätzel, M. Sequential Deposition as a Route to High-Performance Perovskite-Sensitized Solar Cells. *Nature* **2013**, *499*, 316–319.
- (8) Lee, M. M.; Teuscher, J.; Miyasaka, T.; Murakami, T. N.; Snaith, H. J. Efficient Hybrid Solar Cells Based on Meso-Superstructured Organometal Halide Perovskites. *Science* **2012**, *338*, 643–647.
- (9) Liu, M.; Johnston, M. B.; Snaith, H. J. Efficient Planar Heterojunction Perovskite Solar Cells by Vapour Deposition. *Nature* **2013**, *501*, 395–398.
- (10) Baikie, T.; Fang, Y.; Kadro, J. M.; Schreyer, M.; Wei, F.; Mhaisalkar, S. G.; Graetzel, M.; White, T. J. Synthesis and Crystal Chemistry of The Hybrid Perovskite (CH<sub>3</sub>NH<sub>3</sub>)PbI<sub>3</sub> for Solid-State Sensitized Solar Cell Applications. *J. Mater. Chem. A* **2013**, *1*, 5628–5641.
- (11) Im, J.-H.; Lee, C.-R.; Lee, J.-W.; Park, S.-W.; Park, N.-G. 6.5% Efficient Perovskite Quantum-Dot-Sensitized Solar Cell. *Nanoscale* **2011**, *3*, 4088–4093.
- (12) Filip, M. R.; Eperon, G. E.; Snaith, H. J.; Giustino, F. Steric Engineering of Metal-Halide Perovskites with Tunable Optical Band Gaps. *Nat. Commun.* **2014**, *5*, 5757.
- (13) Etgar, L.; Gao, P.; Xue, Z.; Peng, Q.; Chandiran, A. K.; Liu, B.; Nazeeruddin, M. K.; Graetzel, M. Mesoscopic CH<sub>3</sub>NH<sub>3</sub>PbI<sub>3</sub>/TiO<sub>2</sub> Heterojunction Solar Cells. *J. Am. Chem. Soc.* **2012**, *134*, 17396–17399.
- (14) Stoumpos, C. C.; Malliakas, C. D.; Kanatzidis, M. G. Semiconducting Tin and Lead Iodide Perovskites with Organic Cations: Phase Transitions, High Mobilities, and Near-Infrared Photoluminescent Properties. *Inorg. Chem.* **2013**, *52*, 9019–9038.
- (15) Umari, P.; Mosconi, E.; De Angelis, F. Relativistic GW Calculations on CH<sub>3</sub>NH<sub>3</sub>PbI<sub>3</sub> and CH<sub>3</sub>NH<sub>3</sub>SnI<sub>3</sub> Perovskites for Solar Cell Applications. *Sci. Rep.* **2014**, *4*, 4467.
- (16) Geng, W.; Zhang, L.; Zhang, Y.-N.; Lau, W.-M.; Liu, L.-M. First-Principles Study of Lead Iodide Perovskite Tetragonal and Orthorhombic Phases for Photovoltaics. *J. Phys. Chem. C* **2014**, *118*, 19565–19571.
- (17) Du, M. H. Efficient Carrier Transport in Halide Perovskites: Theoretical Perspectives. *J. Mater. Chem. A* **2014**, *2*, 9091–9098.
- (18) Stranks, S. D.; Eperon, G. E.; Grancini, G.; Menelaou, C.; Alcocer, M. J. P.; Leijtens, T.; Herz, L. M.; Petrozza, A.; Snaith, H. J. Electron–Hole Diffusion Lengths Exceeding 1 Micrometer in an Organometal Trihalide Perovskite Absorber. *Science* **2013**, *342*, 341–344.
- (19) Kutes, Y.; Ye, L.; Zhou, Y.; Pang, S.; Huey, B. D.; Padture, N. P. Direct Observation of Ferroelectric Domains in Solution-Processed CH<sub>3</sub>NH<sub>3</sub>PbI<sub>3</sub> Perovskite Thin Films. *J. Phys. Chem. Lett.* **2014**, *5*, 3335–3339.
- (20) Frost, J. M.; Butler, K. T.; Brivio, F.; Hendon, C. H.; van Schilfgaarde, M.; Walsh, A. Atomistic Origins of High-Performance in Hybrid Halide Perovskite Solar Cells. *Nano Lett.* **2014**, *14*, 2584–2590.
- (21) Quarti, C.; Mosconi, E.; De Angelis, F. Interplay of Orientational Order and Electronic Structure in Methylammonium Lead Iodide: Implications for Solar Cell Operation. *Chem. Mater.* **2014**, *26*, 6557–6569.
- (22) Zheng, F.; Takenaka, H.; Wang, F.; Koocher, N. Z.; Rappe, A. M. First-Principles Calculation of Bulk Photovoltaic Effect in



- CH<sub>3</sub>NH<sub>3</sub>PbI<sub>3</sub> and CH<sub>3</sub>NH<sub>3</sub>PbI<sub>3-x</sub>Cl<sub>x</sub>. *J. Phys. Chem. Lett.* **2015**, *6*, 31–37.
- (23) Yang, S. Y.; Seidel, J.; Byrnes, S. J.; Shafer, P.; Yang, C. H.; Rossell, M. D.; Yu, P.; Chu, Y. H.; Scott, J. F.; Ager, J. W.; et al. Above-Bandgap Voltages from Ferroelectric Photovoltaic Devices. *Nat. Nanotechnol.* **2010**, *5*, 143–147.
- (24) Grinberg, I.; West, D. V.; Torres, M.; Gou, G.; Stein, D. M.; Wu, L.; Chen, G.; Gallo, E. M.; Akbashev, A. R.; Davies, P. K.; et al. Perovskites Oxides for Visible-Light-Absorbing Ferroelectric and Photovoltaic Materials. *Nature* **2013**, *503*, 509–512.
- (25) Jo, J.; Yang, S.; Kim, T.; Lee, H.; Yoon, J.-G.; Park, S.; Jo, Y.; Jung, M.; Noh, T. Nonlinear Dynamics of Domain-Wall Propagation in Epitaxial Ferroelectric Thin Films. *Phys. Rev. Lett.* **2009**, *102*, 045701.
- (26) Shin, Y.-H.; Grinberg, I.; Chen, I.-W.; Rappe, A. M. Nucleation and Growth Mechanism of Ferroelectric Domain-Wall Motion. *Nature* **2007**, *449*, 881–886.
- (27) Catalan, G.; Seidel, J.; Ramesh, R.; Scott, J. F. Domain Wall Nanoelectronics. *Rev. Mod. Phys.* **2012**, *84*, 119–156.
- (28) Seidel, J. Domain Walls as Nanoscale Functional Elements. *J. Phys. Chem. Lett.* **2012**, *3*, 2905–2909.
- (29) Liu, S.; Grinberg, I.; Rappe, A. M. Exploration of The Intrinsic Inertial Response of Ferroelectric Domain Walls via Molecular Dynamics Simulations. *Appl. Phys. Lett.* **2013**, *103*, 232907.
- (30) Wojdel, J. C.; Iñiguez, J. Ferroelectric Transitions at Ferroelectric Domain Walls Found from First Principles. *Phys. Rev. Lett.* **2014**, *112*, 247603.
- (31) Xu, R.; Liu, S.; Grinberg, I.; Karthik, J.; Damodaran, A. R.; Rappe, A. M.; Martin, L. W. Ferroelectric Polarization Reversal via Successive Ferroelastic Transitions. *Nat. Mater.* **2015**, *14*, 79–86.
- (32) Seidel, J.; Martin, L. W.; He, Q.; Zhan, Q.; Chu, Y. H.; Rother, A.; Hawkridge, M. E.; Maksymovych, P.; Yu, P.; Gajek, M.; et al. Conduction at Domain Walls in Oxide Multiferroics. *Nat. Mater.* **2009**, *8*, 229–234.
- (33) Farokhipoor, S.; Noheda, B. Conduction through 71° Domain Walls in BiFeO<sub>3</sub> Thin Films. *Phys. Rev. Lett.* **2011**, *107*, 127601.
- (34) Giannozzi, P.; Baroni, S.; Bonini, N.; Calandra, M.; Car, R.; Cavazzoni, C.; Ceresoli, D.; Chiarotti, G. L.; Cococcioni, M.; Dabo, I.; et al. Quantum ESPRESSO: A Modular and Open-Source Software Project for Quantum Simulations of Materials. *J. Phys.: Condens. Matter* **2009**, *21*, 395502.
- (35) Perdew, J. P.; Burke, K.; Ernzerhof, M. Generalized Gradient Approximation Made Simple. *Phys. Rev. Lett.* **1996**, *77*, 3865–3868.
- (36) Rappe, A. M.; Rabe, K. M.; Kaxiras, E.; Joannopoulos, J. D. Optimized Pseudopotentials. *Phys. Rev. B* **1990**, *41*, 1227–1230.
- (37) Ramer, N. J.; Rappe, A. M. Designed Nonlocal Pseudopotentials for Enhanced Transferability. *Phys. Rev. B* **1999**, *59*, 12471–12478.
- (38) Monkhorst, H. J.; Pack, J. D. Special Points for Brillouin-Zone Integrations. *Phys. Rev. B* **1976**, *13*, 5188–5192.
- (39) Meyer, B.; Vanderbilt, D. *Ab Initio* Study of Ferroelectric Domain Walls in PbTiO<sub>3</sub>. *Phys. Rev. B* **2002**, *65*, 104111.
- (40) Mosconi, E.; Amat, A.; Nazeeruddin, M. K.; Graetzel, M.; De Angelis, F. First-Principles Modeling of Mixed Halide Organometal Perovskites for Photovoltaic Applications. *J. Phys. Chem. C* **2013**, *117*, 13902–13913.
- (41) Amat, A.; Mosconi, E.; Ronca, E.; Quarti, C.; Umari, P.; Nazeeruddin, M. K.; Graetzel, M.; De Angelis, F. Cation-Induced Band-Gap Tuning in Organohalide Perovskites: Interplay of Spin–Orbit Coupling and Octahedra Tilting. *Nano Lett.* **2014**, *14*, 3608–3616.
- (42) Even, J.; Pedesseau, L.; Jancu, J.-M.; Katan, C. Importance of Spin–Orbit Coupling in Hybrid Organic/Inorganic Perovskites for Photovoltaic Applications. *J. Phys. Chem. Lett.* **2013**, *4*, 2999–3005.
- (43) Egger, D. A.; Kronik, L. Role of Dispersive Interactions in Determining Structural Properties of Organic–Inorganic Halide Perovskites: Insights from First-Principles Calculations. *J. Phys. Chem. Lett.* **2014**, *5*, 2728–2733.
- (44) Kim, M.; Im, J.; Freeman, A. J.; Ihm, J.; Jin, H. Switchable  $S = 1/2$  and  $J = 1/2$  Rashba Bands in Ferroelectric Halide Perovskites. *Proc. Natl. Acad. Sci. U.S.A.* **2014**, *111*, 6900–6904.
- (45) Heyd, J.; Scuseria, G. E.; Ernzerhof, M. Hybrid Functionals Based on A Screened Coulomb Potential. *J. Chem. Phys.* **2003**, *118*, 8207–8215.
- (46) Heyd, J.; Scuseria, G. E.; Ernzerhof, M. Erratum: “Hybrid Functionals Based on A Screened Coulomb Potential?” [ *J. Chem. Phys.* **118**, 8207 (2003) ]. *J. Chem. Phys.* **2006**, *124*, 219906.
- (47) Sluka, T.; Tagantsev, A. K.; Damjanovic, D.; Gureev, M.; Setter, N. Enhanced Electromechanical Response of Ferroelectrics due to Charged Domain Walls. *Nat. Commun.* **2012**, *3*, 748.
- (48) Ma, J.; Wang, L.-W. Nanoscale Charge Localization Induced by Random Orientations of Organic Molecules in Hybrid Perovskite CH<sub>3</sub>NH<sub>3</sub>PbI<sub>3</sub>. *Nano Lett.* **2015**, *15*, 248–253.
- (49) Gureev, M.; Tagantsev, A.; Setter, N. Head-to-Head and Tail-to-Tail 180° Domain Walls in an Isolated Ferroelectric. *Phys. Rev. B* **2011**, *83*, 184104.
- (50) Egger, D. A.; Edri, E.; Cahen, D.; Hodes, G. Perovskite Solar Cells: Do We Know What We Do Not Know? *J. Phys. Chem. Lett.* **2015**, No. 6, 279–282.
- (51) Cohen, B.-E.; Gamliel, S.; Etgar, L. Parameters Influencing the Deposition of Methylammonium Lead Halide Iodide in Hole Conductor Free Perovskite-Based Solar Cells. *APL Mater.* **2014**, *2*, 081502.
- (52) Lindblad, R.; Bi, D.; Park, B.-w.; Oscarsson, J.; Gorgoi, M.; Siegbahn, H.; Odelius, M.; Johansson, E. M. J.; Rensmo, H. Electronic Structure of TiO<sub>2</sub>/CH<sub>3</sub>NH<sub>3</sub>PbI<sub>3</sub> Perovskite Solar Cell Interfaces. *J. Phys. Chem. Lett.* **2014**, *5*, 648–653.
- (53) Mosconi, E.; Quarti, C.; Ivanovska, T.; Ruani, G.; De Angelis, F. Structural and Electronic Properties of Organo-Halide Lead Perovskites: A Combined IR-Spectroscopy and *Ab Initio* Molecular Dynamics Investigation. *Phys. Chem. Chem. Phys.* **2014**, *16*, 16137–16144.
- (54) Frost, J. M.; Butler, K. T.; Walsh, A. Molecular Ferroelectric Contributions to Anomalous Hysteresis in Hybrid Perovskite Solar Cells. *APL Mater.* **2014**, *2*, 081506.
- (55) Carignano, M. A.; Kachmar, A.; Hutter, J. Thermal Effects on CH<sub>3</sub>NH<sub>3</sub>PbI<sub>3</sub> Perovskite from *Ab-Initio* Molecular Dynamics Simulations. *arXiv preprint arXiv:1409.6842*, 2014.